PAPER

Corrosion behavior of aluminum-Fiber Glass composite fabricated through surface mechanical alloying in alkaline media

Physica Scripta

PAPER

Corrosion behavior of aluminum-Fiber Glass composite fabricated through surface mechanical alloying in alkaline media

RECEIVED
26 February 2021

ACCEPTED FOR PUBLICATION
16 March 2021

PUBLISHED
24 March 2021

O S Shehata[1], **Mohamed Refaat Mohamed Ebrahim**[2] **and Amr H Abdel Fatah**[3]

[1] Physical Chemistry Department, National Research Centre, Dokki, Giza, PO 12622, Egypt
[2] Solid State Department, Physics Division, National Research Centre, Dokki, Giza, PO 12622, Egypt
[3] Faculty of biotechnology, Modern Science and arts university, 6 October city, Giza , Egypt

E-mail: omniashehata@yahoo.com

Keywords: fiber glass, matrix composite, mechanical attrition treatment, surface mechanical alloying, corrosion resistance

Abstract

Dissolution reaction control of aluminum in 2M KOH alkaline media was achieved through surface mechanical alloying SMA with dielectric Fiber glass 'FG' powder. A significant decrease corrosion rate from 0.867 for blank Al to 0.0002 mm y^{-1} for SMA Al with FG powder previously etched after 15 min; surface mechanical attrition treatment 'SMAT'; Formed surface metal matrix Al/FG composites layers on Al anodes have attractive electrical properties. Its analysis obtained using X-Rays Diffraction XRD, scanning electron microscopy SEM. Used three electrochemical techniques EIS, CV and PDP indicate corrosion resistance improvement in 2M KOH correspond to inhibition efficiency reaches 99.81%. Such inhibition encourage for forming efficient and safe air batteries for interesting applications using Al anodes after consecutive SMAT & SMA processing.

1. Introduction

Aluminum usage as anodic material got attention of researchers because of Al electrochemical reaction which converts chemical energy into electricity. Although its high corrosion rate in alkaline media stymied Al-air battery practical applications, so investigations being done on corrosion inhibition [1–4]. Multiple elements were added to Al-air batteries to increase protection like Mg [5], Ga, In, Sn [6–10], Pt [11], Au [12] and Zn [13] were used in protection and $LiCoO_2$ in lithium ion batteries [14] due to their inhibition effect.

Aluminum is an ideal material for metallic fuel cells, different grain sizes of aluminum anodes are is examined by electron backscatter diffraction (EBSD) in scanning electron microscope (SEM). Hydrogen corrosion rates of the Al anodes in 4M l^{-1} NaOH are determined at room temperature . The electrochemical properties are investigated using (EIS) and polarization curves that confirmed that. Finer grain size is improved electrochemical activity and increases anodic utilization rate and is shown to effectively improve the performance of Al-air batteries [15]. The annealing treatment had a certain effect on the number and size of precipitates on the alloy surface, which improved the electrochemical activity and corrosion resistance of the Al alloy [16, 17]. As a result material's crystallographic orientation and grain size influences their electrochemical behavior. Found sever plastic deformation SPD method enables us to get ultra-fine grain structures [18–21], as well as new electrochemical properties [22] and microstructure changes [23–25]. Song *et al* and Gopala *et al* studies on Al alloys supported the avoidance of their localized corrosion [26, 27]. Birbilis *et al* & Gollapudi study on ultra-fine grained pure Al induces passive film formation. Thus corrosion resistance against pitting in Cl^- ions initiate because of Al surface structure with multiple grain boundaries [28, 29]. Last results encourages to use SMA in mixing FG powder with Al enhanced through grain boundaries increase causing mechanical alloying increase with FG. Forming metal matrix composites 'MMCs' that have industrial applications due to their high corrosion resistance and strength [30, 31]. Where passivation on Al surface reaction due to grain refinement initiates increase in resistance against localized corrosion degradation. Moreover dissolution process of aluminum in alkaline solution got technological interest as a relevant anode reaction in aluminum-air batteries [32].

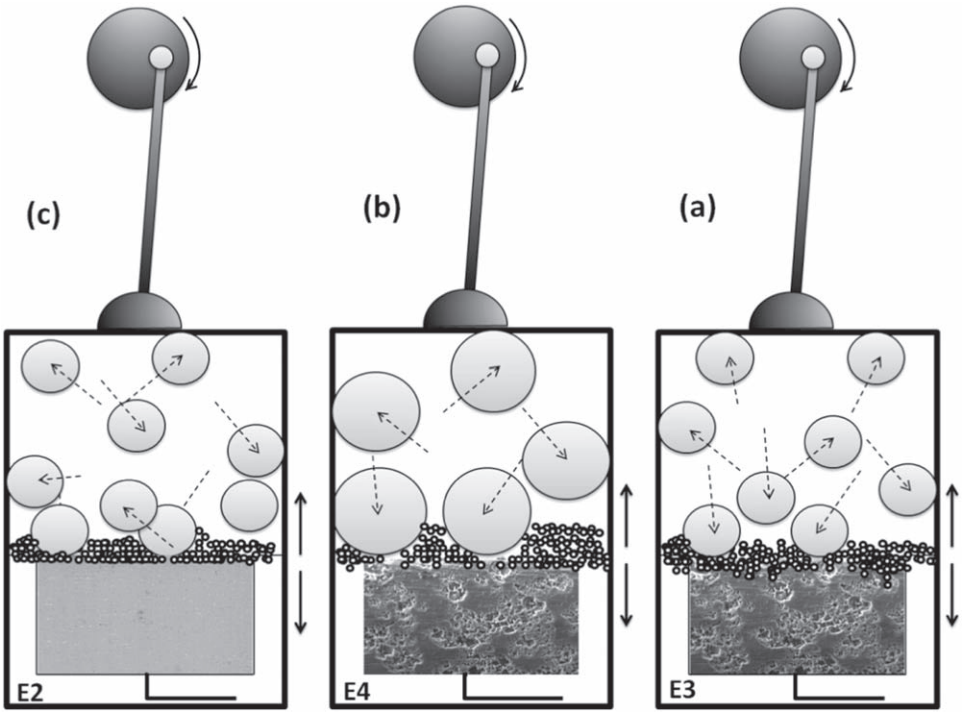

Figure 1. Surface mechanical alloying (SMA) setup used with inset SEM images for metallographic cross sections belong to (a) 'E3', (b) 'E4' and (c) 'E2' Al electrodes.

Our aim directed to prepare compact composite surface layers of Al/FG on Al electrodes fabricated by SMA method and Correlations of its corrosion protection efficiency in alkaline media using electrochemical techniques were studied.

2. Experimental

Commercial Al sheet was cut into four circular electrodes equal in diameters of 2.7 cm. Isothermal annealed two hours at 600 °C covered wrapped inside Al envelopes in muffle furnace. Al electrodes connected with conductive Cu wires and isolated from one side with epoxy molds as seen in 'figures 1(a)–(c)'. All electrodes were surface polished using emery papers till 1500 mesh, used as metal substrates subjected to severe plastic deformation (SPD) using surface mechanical attrition (SMAT) machine. E2, E3 & E4 electrodes surfaces were prepared for mixing with fine powder Fiber glass FG which was grinded from its wool state using manual glass mortar. Surface of E3 & E4 Electrodes were etched using 34% diluted HCl acid after SMAT, Whose metallographic cross sections images impeded inside 'figures 1(a), (b)' after etching for E3 & E4 electrodes respectively. The annealed metallographic non-etched cross section of E2 electrode impeded inside SMA machine's cavity has shown in 'figure 1(c)'. Mixing was done using surface mechanical alloying SMA machine whose cross section seen in 'figure 1'. Alloying parameters were continuously applied for 10 min at 50 Hz vibration, three groups of hard stainless steel balls random impinging on Al and FG powder to induce different alloying conditions. Two groups having 64 balls with equal diameters 1.5 mm were used in alloy mixing on both E2 & E3 electrodes surfaces, meanwhile the third only 8 balls of 6 mm were used in alloy mixing on E4 surface. SMA process starts at the moment the closed SMA cylindrical cavity starts to vibrate, containing the balls and fine FG powder, then process ends when vibration stops. Imposed Frequency was set due to motor's axis circulation connected to a plunger as drawn in 'figure 1'. Comparison between annealed Al electrodes 'E1', 'E2', 'E3' & 'E4' were described in 'table 1'.

Various electrochemical techniques were done using Metrohm Autolab workstation version PGSTAT 302 N, electrochemical cell contain 200 ml of 2M KOH prepared with de-ionized water after a steady state potential reached was used. AC impedance responses were recorded at open circuit potential OCP with a sinusoidal excitation signal 10 mV peak to peak in the frequency range from 0.01 Hz to 100 KHz. Cyclic voltammetry analysis used scan rate of 0.001 V s^{-1} from negative to positive directions in potential range from −0.4 V to 1.0 V. Potentiodynamic polarization curves were obtained at a scan rate of 0.001 V s^{-1} in potential window from −1.4 V to 0.5 V. Corrosion rate mm y^{-1} obtained from data and I/E analysis recorded with Nova software 1.12.

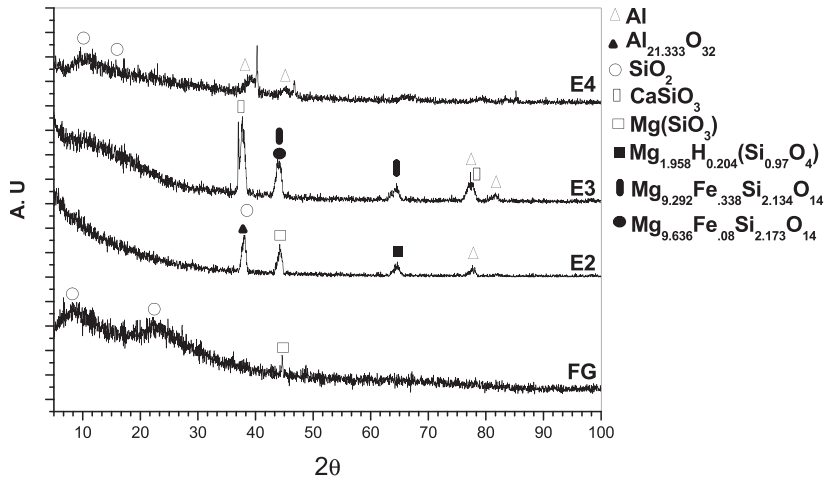

Figure 2. X-Ray Diffraction powder pattern for FG, XRD patterns at grazing incidence for 'E2', 'E3' & 'E4' Al electrodes.

Table 1. Parameters for preparation a compact surface layer of nanoparticles powder of fiber glass on Al electrodes. Tools are surface mechanical attrition treatment (SMAT) and surface mechanical alloying (SMA) adjusted at 50 Hz.

			SMAT condition		Surface SMA condition			
Electrode	E pre-condition.	Surface condition	B. N.	t/min.	t/min.	B. D.	B. N.	Added
E1	Annealed 2 h	Polished						—
(blank)	at 600°C	1000 mesh	—	—	—	—	—	
E2	Annealed 2 h at 600°C	Polished 1000 mesh	—	—	10	1.5	65	FG
E3	Annealed + SMAT	Etched & has micro cavities	33	15	10	1.5	65	FG
E4	Annealed + SMAT	Etched & has micro cavities	33	15	10	6	8	FG

[a] B.D. = Ball Diameter.
[b] B.N. = Number of Balls.

Study of surface morphology of both E3 and E4 electrodes that dried in air after performed EIS, CV and PDP electrochemical techniques in 2M KOH solution. Electrodes morphology of reaction product film covered the surface was seen using a JEOL JXA-840A (QUANTA FEG250) scanning electron probe microscope (Japan) equipped with EDX microanalysis hardware.

3. Results

3.1. Surface mechanical alloying

Prepared Al electrodes have got two different states according to their deformation microstructures as shown in 'figures 1(a)–(c)'. Those states are annealed 'E2' with the lowest deformation state, whereas E3 & E4 are with extremely severe plastic deformed (SPD) state after SMAT then surface etched. Afterwards both E2 & E3 suffered from surface alloying due to random directional bombardments using 1.5 mm diameter hard stainless steel balls. Differently 'E4' suffered from surface alloying due to random directional bombardments using 6 mm diameters hard stainless steel balls. All E2, E3 & E4 electrodes were lid fixed inside SMA plus FG powder addition 'table 1'.

3.2. X-Ray diffraction XRD

'Figure 2' represents X-Rays powder diffraction pattern from manually grinded FG that indicated only SiO_2 phase. FG powder whose initial fibrous structure was reduced into fine powder through grinding, other constituents couldn't be identified appeared after SMA process on E2, E3 & E4 surfaces. Reactions with SiO_2 during SMA process resulted in different phase formation through grazing incidence phase diffraction peaks listed in 'table 2'. Those phases formed due to different mixing extents occur on deformed surfaces.

3.3. Scanning electron microscope SEM

SEM used to manifest the areal view of FG powder fragments, those contains initially formed solid solution products through SMA induced reaction with KOH solution. 'figures 3(a), (b)' show the difference between immersed SMA treated E3 & E4 electrodes using 1.5 mm balls for E3 and 6 mm balls for E4. 'figure 3(c)' shows a small part taken from

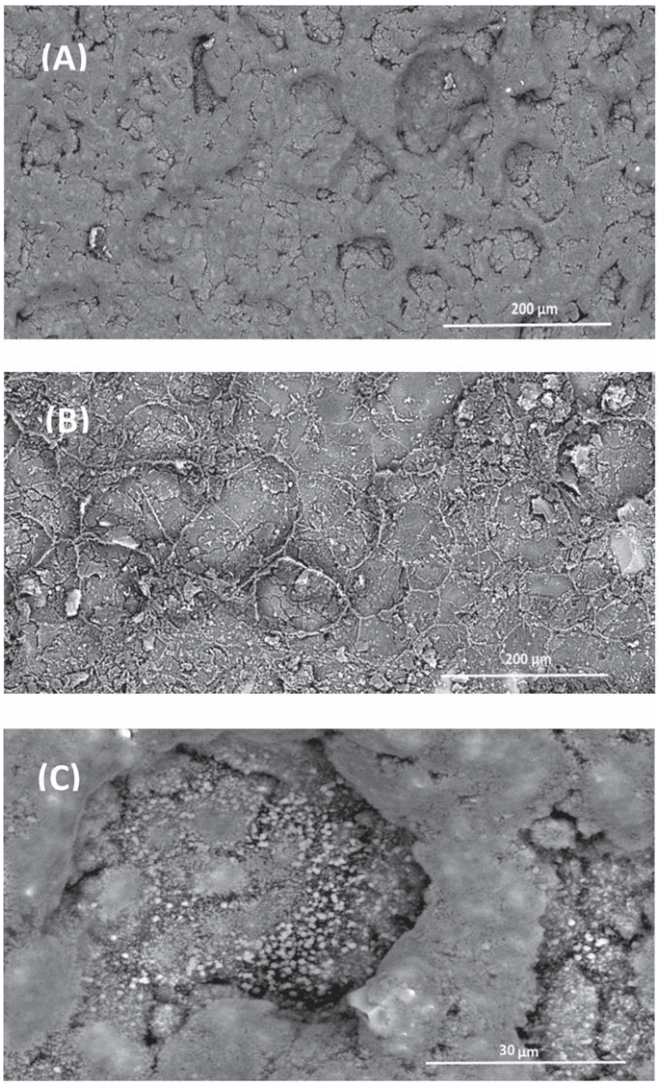

Figure 3. SEM images of reaction product on 'E3' surface (A), surface 'E4' (B) and. magnified micro cavity on 'E3' surface (C).

Table 2. X-Ray diffraction phase identification at grazing incidence on surface reaction layer formed on 'E2', 'E3' and 'E4' electrodes.

Chemical formula: E2	Card no.	Compound Name	Crystal System
$Mg_{1.958}H_{0.204}(Si_{0.97}O_4)$	01–076–2892	Magnesium Hydrogen Silicate	Orthorhombic
$Al_{21.333}O_{32}$	01–080–0955	Aluminum Oxide	Cubic
$Mg(SiO_3)$	01–076–6761	Magnesium Silicon Oxide	Monoclinic
SiO_2	01–075–3168	Silicon Oxide	Hexagonal
Al	01–089–2837	Aluminum	Cubic
Chemical formula:E3			
$Mg_{9.636}Fe_{.08}Si_{2.173}O_{14}$	01–075–3738	Magnesium Iron Silicon	Orthorhombic
$Mg_{9.292}Fe_{.338}Si_{2.134}O_{14}$	01–075–3739	Magnesium Iron Silicon Oxide	Orthorhombic
$Mg(SiO_3)$	01–076–6761	Magnesium Silicon Oxide	Monoclinic
$CaSiO_3$	01–075–5013	Calcium Silicon Oxide	Orthorhombic
CrN	01–076–2494	Chromium Nitride	Cubic
Al	01–073–2661	Aluminum	Cubic
Chemical formula:E4			
SiO_2	01–073–3405	Silicon Oxide	Cubic
Al	01–071–4008	Aluminum	Cubic

'figure 3(a)' reveals open surface micro cavities have picked up FG fragments seen as white spots. The final state formed a reaction product layer of nearly complete coalescence after immersion as seen in 'figure 3(a)'. Whereas the initial FG fibrous structure was still visible on 'E4' surface in 'figure 3(b)', because alloying using 6 mm balls those were

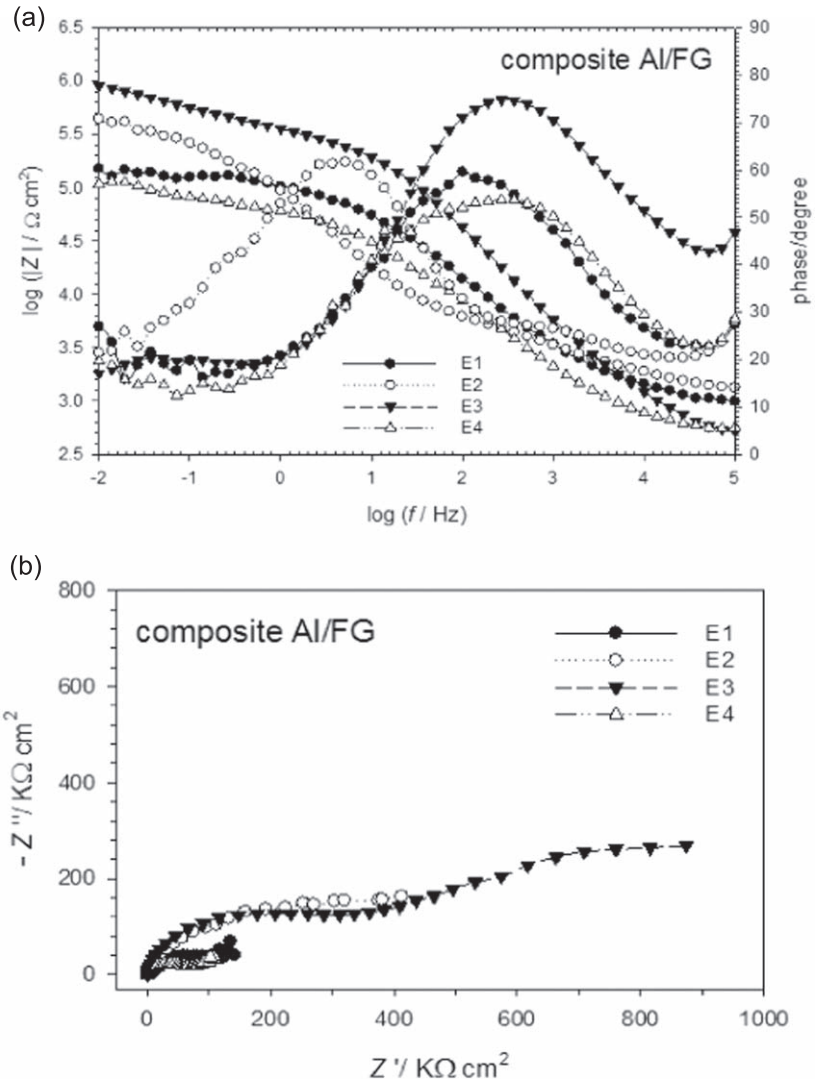

Figure 4. Record of EIS spectrum, (a) Bode plot describes electrode's protection. behavior for 'E1', 'E2', 'E3' & 'E4' Al electrodes. Fig (b) Nyqyist plot shift for 'E3' electrode compared with E1 & E4 followed by 'E2' electrodes.

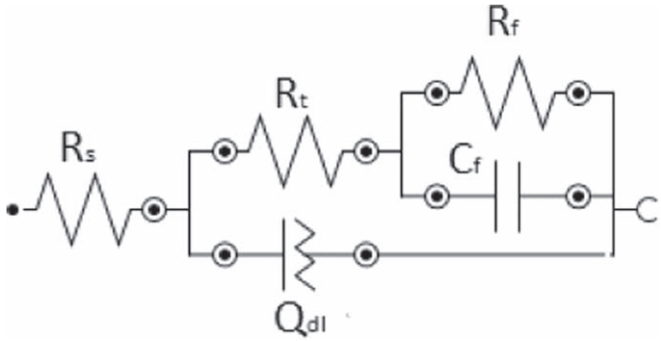

Figure 5. Equivalent circuit model used in the fitting procedure of the EIS data.

exerting less surface localized pressures. Therefore large sized balls inducing negligible picking up by surface open micro cavities and reaction products compared to small sized balls.

3.4. Electrochemical impedance spectroscopy EIS

AC impedance record of 'E1', 'E2', 'E3' & 'E4' spectra depicts the behavior of two layers detected during immersion shown in 'figures 4(a), (b)'. One layer formed at the metal surface due to contact with 2M KOH

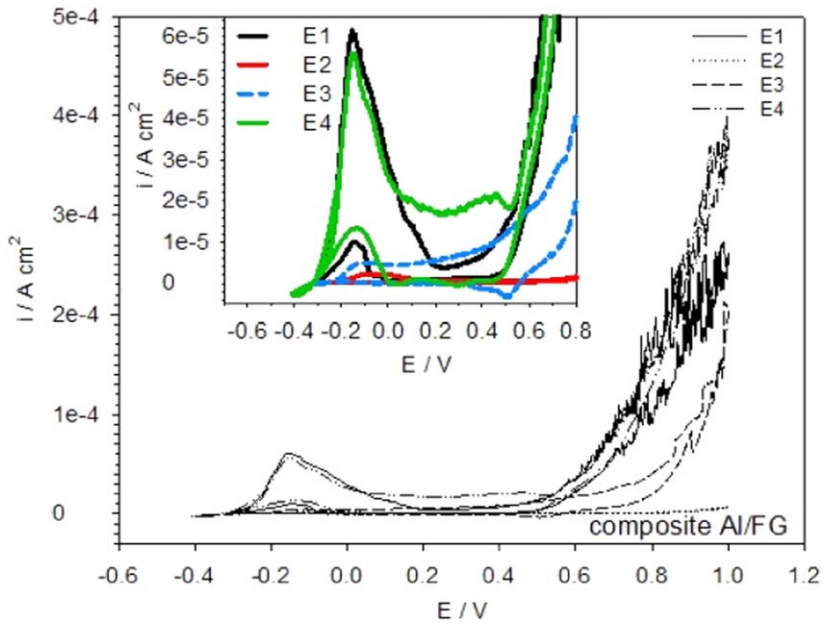

Figure 6. Cyclic Voltametry spectrum describes mass transport process found being. preparation condition for 'E1', 'E2', 'E3' &'E4' electrodes. Inset of CV spectrum inserted in the range from −0.4 to 1.0 E/V for reason of clarity.

Table 3. Simulated parameters of EIS results for investigated electrodes as indicated immersed in alkaline media at room temperature.

Sample	R_t KΩ· cm^2	Q_{dl} μF cm^{-2}	α	R_f KΩ· cm^2	C_f nF·cm^2	R_s Ω· cm^2	R_t R_t+R_f
E1 (blank)	18.3	3.11	0.656	25.2	22.6	271	43.3
E2	106.0	11.4	0.615	50.3	2.30	478	156.3
E3	117.0	0.724	0.745	56.7	1.21	89.6	173.7
E4	3.4	3.84	0.686	22.5	88.8	145	25.9

corrosive media and the other layer due to micro cavities existence in etched Al after SMAT. Their electrochemical behavior of Al composite layer after SMA exhibited high capacitive impedance particularly at high frequencies. Bode plot shows in 'figure 4(a)' as relation between log $|Z|$ recorded and phase angle θ with log f, that describes Nyquist plot of two capacitive loops recorded in 'figure 4(b)'. Their equivalent circuit model drawn in 'figure 5' to evaluate and represents corrosion resistance of resultant corrosion products whose behavior appeared at high frequency as capacitive arc caused by relaxation process of 2M KOH media into fabricated micro cavities. Such relaxation has two dependent parallel time constants included in the model. One due to charge transfer resistance R_t with double layer capacitance Q_{dl} between the investigated electrodes and 2M KOH electrolyte. The other due to R_f in parallel with C_f of interfacial layer that reflects electrochemical and chemical reactions together connected in series with resistance of solution R_s. Therefore double layer capacitance replaced by a constant phase element CPE to obtain satisfactory fitting impedance results. The complex frequency impedance of a constant phase element Z_{CPE} given from 'equation (1)' is due to surface roughness.

$$Z_{CPE} = [Q(i\omega)^{\alpha}]^{-1} \tag{1}$$

where Q is frequency independent parameter, $\omega = 2\pi f$ is angular frequency (rad^{-1}), f frequency and $i = -1^{0.5}$ is the imaginary part [32], α is empirical exponential ranged between zero to one $0 \leqslant \propto \leqslant 1$ related to the surface roughness. All obtained data from fitting are tabulated in 'table 3'.

3.5. Cyclic voltametry CV

CV was scanned from cathodic to anodic direction where current-potential plots are characterized by conduction in film surface indicating interfacial potential between metal and its film coat. Recordings of 'E1', 'E2', 'E3' & 'E4' in 'figure 6' shows initiation of current density rapid increase exhibiting a broad current density maximum between 3 and 60 μA cm^{-2} for E4 & E1, respectively at about −100 mV as listed in 'table 1'. The current decay continues considerably lower till current densities at about 500 mV for all electrodes, such

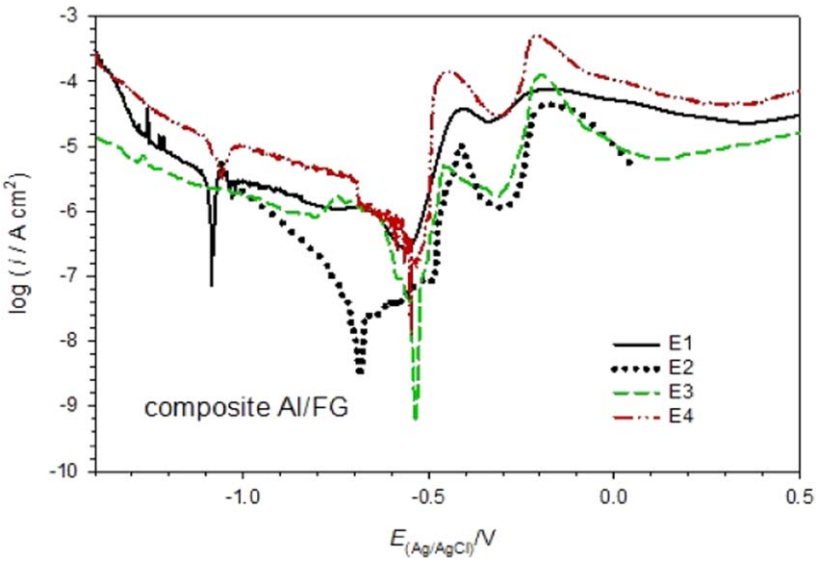

Figure 7. Potential Dynamic Polarization spectrum indicates solution alkalinity that influences 'E1', 'E2', 'E3' and 'E4' surface stability those undergo oxidation reactions depending on surface composite layer's phases contents.

behavior previously observed in Nernest potential for Al oxidation [33]. Currently in case of 'E2', its current density remained lower after 500 mV potential.

3.6. Potentiodynamic polarization PDP

The electrochemical stability of Formed surface metal matrix Al/FG composites layers on Al anodes in 2 M KOH solution was also determined by PDP as represented in 'figure 7'. The electrochemical corrosion parameters obtained from the *E-i* log polarization curves E_{corr} and i_{corr}. Where i_{corr} decrease in the order E3 < E2 < E4 < E1 (High). Corrosion current density i_{corr} and corrosion potential E_{corr} values listed in 'table 4' were obtained by the Tafel extrapolation method. Corrosion rate mm y^{-1} calculated according to 'equation (2)' [34], and estimation of the healing efficiency η % calculated according to 'equation (3)' [35] from the following relationships.

$$CR = \frac{0.00327 \mathrm{xi}_{corr} \mathrm{xE}_{qv}}{d} mm\ \ y^{-1} \tag{2}$$

Where i_{corr} is current density (A cm^{-2}). E_{qv} is equivalent weight (g) and d density;

$$\eta\% = \frac{i_{corr} \times i'_{corr}}{i_{corr}} \times 100\ \ g\ \ cm^{-3}. \tag{3}$$

Where i_{corr} is current density for 'E1' which fabricated film on electrode without FG and i'_{corr} is the current density for 'E2', 'E3' & 'E4' with fine powder FG.

4. Discussions

Thus mixing extents between Al and powder FG on 'E2', 'E3' have been suffering successive local pressures higher than E4 which was suffering low local pressure due to used ball diameters difference from 1.5 mm for 'E2' & 'E3' to 6 mm for 'E4'. In consequence 'E2', 'E3' should have compact surface composite layers with higher mixing extent than E4 between Al and powder FG. Although 'E2' had shallow mixing extent between Al and powder FG due to non-existence of surface micro cavities those played an important role in case of 'E3', 'E4' due to surface etching after SMAT. Thus an increase of mixing extent between Al and FG powder occurs on 'E3' as expected to form a compact surface composite layer.

Such surface composite should be related to its initial deformed state therefore XRD scan was done as shown in 'figure 2'. First pattern depicted SiO_2 peaks at low 2θ after grinding. It seems that FG fiber has reached ultra-fine SiO_2 grains fragments during SMA process with other fragments of little amount that no peaks couldn't be identified with XRD. According to initial composition of used fiber glass [36], only 18 wt% of the fiber is CaO which was finely fragmented into amorphous phase that has no identified peaks. But due to the higher SiO_2 amount exists, the Ca fragments had higher chance to combine with SiO_2 to form $CaSiO_2$ appeared the XRD pattern in

Table 4. Potentiodynamic polarization parameters for investigated electrodes as indicated immersed in alkaline media at room temperature.

Sample	Ba V/dec	βc mV/dec	E_{corr} V	I_{corr} μA cm^{-2}	CR mm year^{-1}	R_{pol} K$\Omega\cdot$ Cm^2	η%
E1 (blank)	4.243	241.54	−1.08	2.653	0.0867	11.92	—
E2	0.109	117.06	−0. 683	0.023	0.0008	341.11	90.77
E3	0.044	23.60	−0. 534	0.005	0.0002	458.95	99.81
E4	0.029	131.38	−0.548	0. 112	0.0037	29.47	95.78

The bivalent cations Ca^{2+}, Mg^{2+}, Fe^{2+} diffuse from the inner volume to the surface, where they react with oxygen from the external medium, forming nano-crystalline layers of CaO, MgO, $(Mg, Fe)_3O_4$ [37].

'Figure 2'. Therefore Second pattern above is XRD at a grazing incidence from annealed Al 'E2' after SMA with FG powder. Shows reactions occurred with KOH solution possibly due to dissociated H_2 atoms from KOH and diffused in FG fragments. That explains the cause of $Mg_{1.958}H_{0.204}$ $(Si_{0.97}O_4)$ plus Mg (SiO_3) formation from initial Mg (SiO_3) as listed in 'table 1'. Moreover peaks from $Al_{21.333}O_{32}$ phase were identified due to oxidation occurred during SMA process of annealed Al 'E2'. Also Mg (SiO_3) fragment phase has broken their SiO_2 groups from Mg atoms whose peaks were identified separately with XRD analysis on 'E2'.

Third pattern from 'E3' depicted $Mg(SiO_3)$ compound associated with insoluble Fe impurity from Al hence $Mg_{9.636}Fe_{.08}Si_{2.173}O_{14}$ and $Mg_{9.292}Fe_{.338}Si_{2.134}O_{14}$ complex phases were identified. Such complex phases formed due to released Fe impurity from Al 'E3' because of weak attraction forces between Al and Fe during SMA process, thus Fe atoms were easily picked up by surface reaction product layer.

SMA process factors made differences between 'E3', 'E2' and 'E4' after processing; those are, the existence of numerous open volume surface defects 'micro cavities' on 'E3' compared to 'E2' whose surface has no micro cavities. The use of small sized balls of 1.5 mm in diameter on 'E3' compared with larger 6 mm balls on 'E4'. Such factors resulted not only in an increase of mixing on Al with FG fragments during SMA process, but also to change the composition of surface composites. Hence 'E4' electrode had only SiO_2 phase from FG powder plus Al those were detected without any mixing on 'E4' surface. Due to less localized pressures exerted on SiO_2 phase during SMA with large ball sizes inducing less work in mixing between SiO_2 and Al. Complex compounds formation were identified only on 'E3' and 'E2' surfaces and simple structures identified on 'E1' & 'E4' surfaces. Also, $CaSiO_3$ phase existence of minority phase ' table 2' formed in surface composite on 'E3', who was reported to increase corrosion resistance if existed in surface composite layers [38].

Electrode's protection behavior indicated by high $|Z|$ at low frequency and constant phase angle shift at the highest frequency for 'E3' compared with 'E1' & ' E4' followed by 'E2' was recorded by their EIS spectrum in 'figure 4(a)' indicating better corrosion resistance. Explained due to current outflow limited through barrier layers those formed because of micro cavity. Two capacitive loops appeared in 'figure 4(b)' one at high frequency due to redox reactions $Al \leftrightarrow Al^+$ being assumed rate determining of charge transfer process [39]. The other appeared at low-frequency attributed due to further redox reaction $Al^+ \leftrightarrow Al^{3+}$.

Mass transport process being preparation condition 'table 1' dependent described through its CV spectrum for each electrode shown in 'figure 6'. Its behavior depends on formed surface compact layers on Al due to SMA processing and formed phase indicated by XRD. Therefore varied behavior of E1and 'E4' continues as fluctuations occur due to hydrogen evolution and oxygen reduction. While Al electrode self-protection depends on oxidation till forming highly resistive surface film with a great ionic conduction. Anodic dissolution of Al occurs in 2M KOH media by sub-micrometer AlH_3 particles participation at room temperature [40]. Also, as a hydride layer in contact with Al has formed may precipitate $Al(OH)_3$ during alkaline dissolution [41, 42].

PDP spectrum recorded in 'figure 7' indicates solution alkalinity that influences 'E3' and 'E4' surface stability, meanwhile oxidation reactions occur depending on surface composite layer's contents. Moreover 'E3' & 'E4' cathodic branches record current densities agrees with their EIS behavior recorded in 'figure 4'. Such behavior should be due to formed compact surface composite layer contains $CaSiO_3$ on E3 compared to E4 with SiO_2 and Al. Whereas 'E3' characterized by a lowest current density 0.20 μA with shifting towards less negative corrosion potentials near E_{corr} −550 mV. While 'E1' was recorded 82 μA compared to 0.21 μA, 1.38 μA for 'E2' & 'E4' respectively. Concluding that higher corrosion resistance for 'E3' than 'E2' & 'E4' was recorded due to $CaSiO_3$ phase content. Corrosion current showed decrease abruptly forming a peak then increasing again. Therefore two current peaks were observed as the potential swept to more positive values due to electrochemical reaction by the end potential window with a continuous plateau afterwards current density decreases. Last continuous plateau is attributed to composite layer product had oxidation to form stable aluminate ions. Last behavior represents a trend of decrease due to de-passivation and re-passivation that advantages Al electrodes to have a self-healing surface layer without revealed domain of passivity. Thus a state of active surface was evidenced by maximum current reached at −350 mV that was recorded in CV spectrum in 'figure 6'.

Formed product layer induced consecutive peaks due to passivation followed by dissolution then replaced by a current plateau after E_{corr} equals zero in attempt for re-passivation. An interpretation for such behavior is current density limitation as electrode's surface being covered with aluminum hydroxide after its surface open volume defects (micro cavities) was already filled with hydroxyl particles [32].

Significant decrease in corrosion rate observed for 'E3' than 'E1' (annealed Al) according to equation (2) that seems like inhibition action for 'E3' against electrochemical reaction with KOH ions. Maximum efficiency reached 99.81% calculated for E3 according to equation (3) means that passivation resistance strengthening ensures the stability of formed film contrary to 'E1' without micro cavities. 'E3' homogeneous Al_2O_3 film growth was through simultaneous migration of OH^- ions and Al oxidized atoms helped by electric field generated across the film due to applied potential. The aluminum hydride formation was one of the major products from aluminum dissolution process and hydrogen evolution as we propose the following a reaction mechanism.

4.1. Mechanism of protection effect

Anodized was deformed aluminum being positively polarized, As a result of electrochemical dissolution, while Al_2O_3 reacts with KOH forming $Al(OH)_4^-$ stable ions according to 'equations (4)–(10)'.

$$Al \rightarrow Al^{3+} + 3e^- \tag{4}$$

$$O_2 + 2H_2O + 4e^- \rightarrow 4OH^- \tag{5}$$

$$4Al + 3O_2 + 6H_2O \rightarrow 4Al(OH)_3 \tag{6}$$

$$Al + 3H \rightarrow AlH_3 \tag{7}$$

$$Al(OH)_3 + KOH \rightarrow Al(OH)_4^- + K^+ \tag{8}$$

The overall dissolution reactions lead to form of hydroxide $Al(OH)_3$ layer, that compete between stable aluminate ions $Al(OH)_4^-$ moreover, the aluminate hydride AlH_3 as products [43]. The concentration $Al(OH)_4^-$ found near the aluminum surface is expected to increase with time until the solubility of $Al(OH)_3$ was reached. As well as it promote the association of the particles to AlH_3 rather than $Al(OH)_3$.

Generally, the electrochemical and chemical processes occurred at 'E2', 'E3' & 'E4' electrodes with Al/FG composite layers can be summarized as follows;

$$Al_{(cs)} + OH^- \rightarrow Al(OH)_{ads} + e^- \tag{9}$$

Where (cs) represents the composite surface active sites. And chemical processes according to equation (10)

$$Al(OH)_{ads} + 3OH^- \rightarrow Al(OH)_4^- \tag{10}$$

Surface mixing with FG powder helped by surface micro-cavities and influence of corrosion product solubility. Thus effective self-healing action introduced because of preventive action against corrosive KOH contact [44].

The major alloying composite of silicon accumulate near the surface of electrodes affect via forming electrochemically active phases. Since Si is more-noble than aluminum its accumulation near the metal/film surface during alkaline dissolution can affect the corrosion potential. Its higher content is cathodically active and thus anodically polarized the aluminum as agree with electrochemical results.

In case of E4 electrode's surface formed with 6 mm balls during SMA those exerted low pressures and shallow mixing resulted only in SiO_2 phase formation. Thus higher solubility of corrosion product occurred on 'E4' electrode which had little mixing resulted due to large ball's diameters than 'E3'. A quick leach of stable $Al(OH)_4^-$ ions out of micro cavities those considered as adsorbing sites helped through capillary forces. Where the ability to flow towards narrow cavities increase inside surface composite matched previously by other workers [45–47]. Therefore active corrosion had been taking place in KOH solution. Contrary to 'E3' electrode's surface formed with 1.5 mm balls those exerted higher pressures and higher surface mixing thus induce lower solubility of corrosion products those resulted in lower corrosion. Therefore increased successive pressures on FG particles those inserted inside micro-cavities thus leads to a lack of corrosion active sites on surfaces, it was become stable due to the fiber glass bridging effect [48]. Concluding that corrosion product precipitates on surface composite would reduce the effect of KOH solution.

5. Conclusion

Surface mechanical attrition treatment SMAT of Al electrodes before surface mechanical alloying SMA has tremendous effect on its electrochemical behavior. Al deformation microstructure containing open volume micro cavities can control its electrochemical behavior. Formed phases after immersion got complex compositions between Al and FG fragments, they are strongly restrained corrosive ions transport. Diameter of balls used in SMA cavity can control the surface alloying product which reflects on corrosion resistance after

immersion in KOH. These parameters are imposed control protection efficiency (η) up to 99.81% of through formed corrosion product layer.

Data availability statement

All data that support the findings of this study are included within the article (and any supplementary files).

ORCID iDs

O S Shehata https://orcid.org/0000-0001-8134-2675
Amr H Abdel Fatah https://orcid.org/0000-0002-0566-125X

References

[1] Shao H B, Wang J M, Zhang Z, Zhang J Q and Cao C N 2003 The cooperative effect of calcium ions and tartrate ions on the corrosion inhibition of pure aluminum in an alkaline solution *Mater. Chem. & Phys.* **77** 305–9
[2] Tang Y, Lu L, Roesky H W, Wang L and Huang B 2004 The effect of zinc on the aluminum anode of the aluminum–air battery *J. of P. Sources.* **138** 313–8
[3] Abiola O K and Otaigbe J O E 2009 The effects of Phyllanthus amarus extract on corrosion and kinetics of corrosion process of aluminum in alkaline solution *Corr. Sci.* **51** 2790–3
[4] Irshedat M K, Nawafleh E M, Bataineh T T, Muhaidat R, Al-Qudah M A and Alomary A A 2013 Investigations of the inhibition of aluminum corrosion in 1 M NaOH solution by lupinus varius l, extract *Portugaliae Electrochimica Acta* **31** 1–10
[5] Song G-L, Mishra R and Xu Z Q 2010 Crystallographic orientation and electrochemical activity of AZ31 Mg alloy *Electrochem. Commun.* **12** 1009–12
[6] Ma J L and Wen J B 2014 Performance of Al-0.5 Mg-0.02 Ga-0.1 Sn-0.5 Mn as anode for Al-air battery in NaCl solutions *J. Electrochem. Soc.* **161** A376–80
[7] Gudic S, Radosevic J, Smoljko I and Kliskic M 2005 Cathodic breakdown of anodic oxide film on Al and Al–Sn alloys in NaCl solution *Electrochim. Acta* **50** 5624–32
[8] Ambat R, Davenport A J, Scamans G M and Afseth A 2006 Effect of iron-containing intermetallic particles on the corrosion behavior of aluminum *Corros. Sci.* **48** 3455–71
[9] Smoljko I, Gudic S, Kuzmanic N and Kliskic M 2012 Electrochemical properties of aluminium anodes for Al/air batteries with aqueous sodium chloride electrolyte *J. Appl. Electrochem.* **42** 969–77
[10] Wilhelmsen W, Arnesen T, Hasvold O and Størkersen N J 1991 The electrochemical behavior of Al-In alloys in alkaline electrolytes *Electrochim. Acta* **36** 79–85
[11] Lu L *et al* 2008 Electrochemical behaviors of dimethyl ether on platinum single crystal electrodes. Part I: Pt (111) *J. Electroanal. Chem.* **619–620** 143–51
[12] Hu Y, Zhang J and Ulstrup J 2011 Investigation of *Streptococcus mutans* biofilm growth on modified Au(111)-surfaces using AFM and electrochemistry *J. Electroanal. Chem.* **656** 41–9
[13] Wang H *et al* 2006 Electrochemical performance of Zn(002) and Zn(100) Single Crystals in 6.0 mol.L-1 KOH *J. Chem. Eng.* **14** 551–4
[14] Shim J-H, Cho S-W, Missiul A and Lee H-O J S 2015 Facial-shape controlled precursors for lithium cobalt oxides and the electrochemical performances in lithium ion battery *J. P. Sources* **274** 659–66
[15] Fan L and Lu H 2015 The effect of grain size on aluminum anodes for Al-air batteries in alkaline electrolytes *J. of Power Sources* **284** 409–15
[16] Han Z, Xu Y, Zhou S, Xu L and Zhu P 2020 The effect of annealing on electrochemical performances of an Al–Sn–Ga–Mg alloy as an anode for al–air batteries in alkaline electrolytes *J. Electrochem. Soc.* **167** 100541
[17] Fan L and Lu H 2015 Performance of fine structured aluminum anodes in neutral and alkaline electrolytes for Al-air batteries *Electrochim. Acta* **165** 22–8
[18] Lowe T C and Valiev R Z (ed) 2000 *Investigations and Applications of Severe Plastic Deformation* (Dordrecht, The Netherlands: Kluwer Academic Publishing) p. 395
[19] Valiev R Z and Alexandrov I V 2000 *Nanostructured Materials Obtained by Severe Plastic Deformation* (Moscow: Logos) p. 267–72
[20] Kapoor R 2017 severe plastic deformation of materials *Materials Under Extreme Conditions, Recent Trends and Future Prospects* (Elsevier) ch 20 717–54 (www.sciencedirect.com/science/article/pii/B9780128013007000206)
[21] Quan G Z, Mao Y P, Li G S, Lv W Q, Wang Y and Zhou J 2012 A characterization for the dynamic recrystallization kinetics of as-extruded 7075 aluminum alloy based on true stress-strain curves *Comp. Mat. Sci.* **55** 65–72
[22] Senkov O, Froes F, Stolyarov V, Valiev R and Liu J 1998 Microstructure of aluminum-iron alloys subjected to severe plastic deformation *Scr. Mater.* **38** 1511–6
[23] Zhao F X, Xu X C, Liu H Q and Wang Y L 2014 Effect of annealing treatment on the microstructure and mechanical properties of ultrafine-grained aluminum *Mat. Design* **53** 262–8
[24] Ma K *et al* 2014 Mechanical behaviour and strengthening mechanisms in ultrafine grain precipitation strengthened aluminum alloy *Acta Mater.* **62** 141–55
[25] Song D, MA A, Jiang J, Lin P and Yang D 2009 Corrosion behaviour of ultra-fine grained industrial pure Al fabricated by ECAP *Trans. of N-ferrous Met. Soc. of China* **19** 1065–70
[26] Krishna K G, Sivaprasad K, Narayanan T S N S and Kumar K C H 2012 Localized corrosion of an ultrafine grained Al-4Zn-2Mg alloy produced by cryorolling *Corr. Sci.* **60** 82–9
[27] Ralston K D, Birbilis N and Davies C H J 2010 Revealing the relationship between grain size and corrosion rate of metals *Scr. Mater.* **63** 1201–4
[28] Gollapudi S 2012 Grain size distribution effects on the corrosion behavior of materials *Corr. Sci.* **62** 90–4
[29] Sharma P, Bhanot V K, Singh D, Undal H S and Sharma M 2013 Research work on fiber glass wool reinforced and epoxy matrix composite material *Int. J. of Mech. Eng. & Robotics Res.* **2** 106–24

[30] Al-Salihi H A and Judran H K 2020 Effect of Al_2O_3 reinforcement nanoparticles on the tribological behaviour and mechanical properties of Al6061 alloy *AIMS Materials Science* **7** 486–98
[31] Man H C, Leong K H and Ho K L 2008 Process monitoring of powder pre-paste laser surface alloying *Optics & Lasers in Eng.* **46** 739–45
[32] Ebrahim M R, Shehata O S and Abdel Fatah A H 2019 Electrochemical behavior of $Al2O_3$/Al composite coated Al electrodes through surface mechanical alloying in alkaline media *Cur. Appl. Phys.* **19** 388–93
[33] Pourbaix M 1974 *Atlas of Electrochemical Equilibria in Aqueous Solutions* (Houston, Texas: Pergamon)
[34] Loto R T and Adeleke A 2016 Corrosion of aluminum alloy metal matrix composites in neutral chloride solutions *J. Fail. Anal. and Preven* **16** 874–85
[35] Chaubey N, Singh V K, Savita M A Q and Ebenso E E 2015 Corrosion inhibition of aluminium alloy in alkaline media by neolamarkia cadamba bark extract as a green inhibitor *Int. J. Electrochem. Sci.* **10** 504–18
[36] Sathishkumar T P, Satheeshkumar S and Jesuarockiam N 2014 Glass fiber-reinforced polymer composites - a review *J. Reinf. Plast. Compos.* **33** 1258–75
[37] Lebedev M P, Startsev O V and Kychin A K 2020 Kychkin the effects of aggressive environments on the mechanical properties of basalt plastics *Heliyon.* **6** e03481
[38] Singh A, Ahamad I and Quraishi M A 2016 Piper longum extract as green corrosion inhibitor for aluminum in NaOH solution *Arabian J. Chem.* **9** S1584–9
[39] Matsuzaki A, Nagoshi M, Noro H, Yamashita M and Hara N 2011 Self-healing effect by zinc phosphate and calcium silicate included in organic-inorganic composite coating on 55% Al-Zn coated steel sheet *Mat. Trans.* **52** 1244–51
[40] Winkler A, Resch C and Rendulic K D 1991 Aluminum hydride desorption from hydrogen covered aluminum single crystal surfaces *J. Chem. Phys.* **95** 7682
[41] Adhikari S, Lee J and Hebert K R 2008 Formation of aluminum hydride during alkaline dissolution of aluminum *J. Electrochem. Soc.* **155** C16–21
[42] Greef R and Norman C F W 1985 Ellipsometry of the growth and dissolution of anodic oxide films on aluminum in alkaline solution *J. Electrochem. Soc.* **132** 2362–9
[43] Brown O R and Whitley J S 1987 Electrochemical in aqueous caustic solutions *Electrochim. Acta* **32** 545–56
[44] Doche M L, Rameau J J, Durand R and Novel-Cattin F 1999 Electrochemical behaviour of aluminium in concentrated NaOH solutions *Corr. Sci.* **41** 805–26
[45] Shchukin D and Zheludkevich M 2006 Layer-by-layer assembled nanocontainers for self-healing corrosion protection *Adv. Mater.* **18** 1672–8
[46] Lamaka S and Zheludkevich M 2007 Nanoporous titania interlayer as reservoir of corrosion inhibitors for coatings with self-healing ability *Prog. in Org. Coat.* **58** 127–35
[47] Liu L and Hu J 2006 Improving the formation and protective properties of silane films by the combined use of electrodeposition and nanoparticles incorporation *Electrochim. Acta* **52** 538–45
[48] Wu X *et al* 2020 Synergistic delamination toughening of glass fiber-aluminum laminates by surfacetreatment and graphene oxide interleaf *Nanoscale Res. Lett.* **15** 1–14